Astronomy & Astrophysics manuscript no. 13455ms
November 25, 2009

The interface between the stellar wind and interstellar medium around R Cassiopeiae revealed by far-infrared imaging⋆

Toshiya Ueta[1], Robert E. Stencel[1], Issei Yamamura[2], Kathleen M. Geise[1], Agata Karska[3,4], Hideyuki Izumiura[5], Yoshikazu Nakada[6], Mikako Matsuura[7,8], Yoshifusa Ita[2,9], Toshihiko Tanabé[6], Hinako Fukushi[6], Noriyuki Matsunaga[6], Hiroyuki Mito[10], and Angela K. Speck[11]

(Affiliations can be found after the references)

Received 14 October 2009/ Accepted 12 November 2009

ABSTRACT

Aims. The circumstellar dust shells of intermediate initial-mass ($\sim$ 1 to 8 $M_\odot$) evolved stars are generated by copious mass loss during the asymptotic giant branch phase. The density structure of their circumstellar shell is the direct evidence of mass loss processes, from which we can investigate the nature of mass loss.

Methods. We used the *AKARI Infrared Astronomy Satellite and the Spitzer Space Telescope to obtain the surface brightness maps of an evolved star R Cas at far-infrared wavelengths, since the temperature of dust decreases as the distance from the star increases and one needs to probe dust at lower temperatures, i.e., at longer wavelengths. The observed shell structure and the star's known proper motion suggest that the structure represents the interface regions between the dusty wind and the interstellar medium. The deconvolved structures are fitted with the analytic bow shock structure to determine the inclination angle of the bow shock cone.*

Results. Our data show that (1) the bow shock cone of $1-5\times10^{-5}$ $M_\odot$ *dust mass is inclined at* 68° *with respect to the plane of the sky, and (2) the dust temperature in the bow shock cone is raised to more than 20 K by collisional shock interaction in addition to the ambient interstellar radiation field. By comparison between the apex vector of the bow shock and space motion vector of the star we infer that there is a flow of interstellar medium local to R Cas whose flow velocity is at least 55.6 km* s^{-1}*, consistent with an environment conducive to dust heating by shock interactions.*

Key words. Circumstellar matter — Infrared: stars — Stars: AGB and post-AGB — Stars: individual (R Cas) — Stars: mass loss — ISM: kinematics and dynamics

1. Introduction

Numerous observations have elucidated the magnitude and ubiquity of mass loss across the upper-right side of the Hertzsprung-Russell diagram in the fifty years since Deutsch (1956) discussed the existence of blue-shifted circumstellar cores in the spectrum of the red supergiant star α Her, which constituted one of the first pieces of direct evidence for high rates of mass loss. Since such high rates of mass loss among asymptotic giant branch (AGB) stars rival evolutionary timescales and substantially affect stellar evolutionary tracks, careful investigations into mass loss from these stars are indeed necessary. Moreover, since mass loss defines the boundary conditions for stellar evolutionary tracks, the rate of mass loss from these stars is hardly time-invariant. These facts have had theorists perplexed, who are struggling with the basic challenge of how to lift so much mass away from the gravitational hold of the star (e.g. Gustafsson & Höfner 2004).

Observations made with the *Infrared Astronomical Satellite* (*IRAS*) during the 1980's in the far-infrared (far-IR) have demonstrated that extended shells of evolved stars – the anticipated effect of continuous dusty mass loss – were present (e.g. Stencel et al. 1988; Young et al. 1993a). During the 1990s, the *Infrared Space Observatory* (*ISO*) and ground-based IR work began to refine those results (e.g. Izumiura et al. 1997; Meixner et al. 1999), indicating variations in the mass loss rate over time that resulted in multiple shells and axisymmetric structures. This decade, we are fortunate to have new instruments with higher resolution and sensitivity, such as the *AKARI Infrared Astronomy Satellite* (*AKARI*, formerly known as *ASTRO-F*; Murakami et al. 2007) and the *Spitzer Space Telescope* (*Spitzer*; Werner et al. 2004) that can more carefully map out the mass loss history of evolved stars.

In parallel with investigations into the mass loss history of evolved stars, evidence of interactions between the circumstellar matter and interstellar medium (ISM) around AGB stars is growing, with new observations of bow shocks around R Hya (Ueta et al. 2006) and Mira (Martin et al. 2007; Ueta 2008), plus theoretical considerations of the phenomena (e.g. Villaver et al. 2003; Wareing et al. 2007). This report is one of the first of several studies of well-resolved extended circumstellar dust shells of AGB stars under *AKARI* and *Spitzer* observing programs labeled "Excavating Mass Loss History in Extended Dust Shells of Evolved Stars" (MLHES). In this paper, we explore the detection of an arcminute-sized dust shell around the oxygen-rich AGB star, R Cassiopeiae (HD 224490; hereafter R Cas), in context of interactions between the AGB wind from R Cas and the ISM.

2. R Cas: the Star and its Circumstellar Dust Shell

The Mira type variable, R Cas, is an oxygen-rich, M7IIIe star with a period of 431 days (Kukarkin et al. 1969) and estimated mass loss rate of 5×10^{-7} $M_\odot$ yr^{-1} (Knapp & Morris 1985). This star is known to show an extended circumstellar shell orig-

⋆ Based in part on observations with *AKARI*, a JAXA project with the participation of ESA, and with the *Spitzer Space Telescope*, which is operated by the Jet Propulsion Laboratory, California Institute of Technology under a contract with NASA.

inally detected by *IRAS* at 60μm, having angular extent up to 4.′3 (Young et al. 1993a). Bauer & Stencel (1994) later reported the angular size of 2.′8 using deconvolution of the point-spread-function (PSF). The linear extent of the shell depends on the distance determination.

Hipparcos (Perryman et al. 1997) measured a parallax for R Cas to be 9.37 ± 1.10 milli-arcseconds (mas), corresponding to 107 ± 13 pc. A new calculation done by van Leeuwen (2007) yielded 7.95 ± 1.02 mas, corresponding to 127 ± 16 pc. Other authors prefer values as small as 100 pc (Pourbaix et al, 2003; Knapp et al. 2003) or as large as 220 pc (Knapp & Morris 1985). *Hipparcos* also detected a 10 mas shift of the centroid of the star, whose time-dependent, asymmetric size was determined interferometrically to be 20-40 mas diameter (Hofmann et al. 2001). Since the rotation of a bright stellar spot, for example, could increase the apparent parallax value, the *Hipparcos* measurement for the distance to R Cas is more uncertain than the quoted error values above. Vlemmings et al. (2003) performed VLBI astrometry and obtained a significantly smaller parallax value (5.67 ± 1.95 mas) for R Cas with respect to the *Hipparcos* measurement. Their analysis suggests the distance of 176^{-92}_{+45} pc. This maser astrometry value is more in line with the larger distance estimate of 160 pc inferred from the Period-Luminosity relations (Haniff et al. 1995). Since an ensemble of VLBI measurements over a long time-basis is less affected by uncertainties induced by changes on smaller time scales that probably affected *Hipparcos* measurements, we will adopt the VLBI distance measurement of 176 pc for our purposes.

3. Far-IR Observations of R Cas

3.1. AKARI FIS Imaging

We observed R Cas in the four bands at 65, 90, 140 and 160μm with the Far-Infrared Surveyor (FIS; Kawada et al. 2007) onboard *AKARI* on 2007 January 16 as part of the *AKARI*-MLHES Mission Program (PI: I. Yamamura). Observations were made with the FIS01 (compact source photometry) slow-scan mode, in which two linear strips of forward and backward scans were performed with a 70″ spacing between the scan strips at the 15″ s^{-1} scan rate with a reset rate of 0.5 sec, resulting in the sky coverage of roughly 10′ × 50′ centered at the target.

The FIS Slow-Scan Toolkit (ver. 20070914[1]; Verdugo et al. 2007) was used to reduce the data. We found that the quality of the resulting map was improved when we used a temporal median filter with the width of 200 s (or longer), a temporal boxcar filter with the width of 90 s, and the sigma clipping threshold of 1.5. For the reduction of data in the short wavelength bands (at 65 and 90μm), the results were also improved when we performed flat-fielding of the data using the local "blank" sky data.

The resulting maps are in 15″ and 30″ pixel^{-1} (nominal scale) for the short wavelength (65 and 90μm; SW) and long wavelength (140 and 160μm; LW) bands, respectively, with the average of 6, 9, 15, and 10 sky coverages per pixel at 65, 90, 140 and 160μm, respectively. The resulting 1 σ sensitivities and the average sky emission (the component removed by median filtering during the reduction) are found to be 1.2, 0.6, 1.3 and 1.3 MJy sr^{-1} and 8.7 ± 0.3, 8.6 ± 0.1, 13.2 ± 0.3 and 9.9 ± 0.3 MJy sr^{-1} at 65, 90, 140 and 160μm, respectively. Characteristics of the *AKARI* observations and images are summarized in Table 1: images themselves are shown in the top row of Figure 1.

3.2. Spitzer MIPS Imaging

R Cas observations at 70μm by *Spitzer* was made with the Multiband Imaging Photometer for *Spitzer* (MIPS; Rieke et al. 2004) on 2008 February 18 as part of the *Spitzer*-MLHES project (PI: T. Ueta). Observations were done in the photometry/fixed-cluster-offset mode, in which a series of 12 exposures were made in a spiral pattern around R Cas. This exposure pattern was intended not to allow the bright central star fall on the 70μm Ge:Ga detector array in "prime" and on the 24μm Si:As detector array in "non-prime" in order to avoid saturation and severe transient effects due to the central star. In effect, we achieved the sky coverage of 13′ × 22′ centered at the target (but the central 3′ × 1.8′ around the star is unobserved).

For the data reduction, we started with the basic calibrated data (BCD), which are relatively free from instrumental artifacts. However, to optimize the detection of intrinsically faint extended shells we used a custom IDL script to remove time- and pixel-dependent instrumental effects still remaining in the BCD. This script was developed originally to reduce similar MIPS data obtained in the MIPS IR Imaging of AGB Dust shells (MIRIAD) project (PI: A. K. Speck), based on the idea that it is highly unlikely that there arises any periodicity in the time-series pixel readings given the way the *Spitzer* aperture was dithered around in the target region. This extra BCD cleaning has proven to be effective in correcting those residual instrumental effects and removing residual background sky emission (cf. Ueta et al. 2006). We then used the MOsaicker and Point source EXtractor (MOPEX) software (ver. 20080819[2]; Makovoz et al. 2006) to produce a final mosaicked image.

The resulting map is in 4.″92 pixel^{-1} (sub-pixelized by a factor of 2 from the nominal scale) with the average of 9, and up to 24, sky coverages per pixel. The 1 σ sensitivity and the average sky emission (the component removed during the reduction) are found to be 1.1 MJy sr^{-1} and 10.0 ± 0.7 MJy sr^{-1}, respectively. Characteristics of the *Spitzer* observations and image are summarized in Table 1: image itself is shown in the top-left frame of Figure 2.

3.3. Photometry and Deconvolution

Photometry was done only with the AKARI images that capture the circumstellar shell for its entirety. Because the absolute calibration of the FIS Slow-Scan data is based on the measurements of the diffuse sky emission from zodiacal light and interstellar cirrus done by CODE/DIRBE measurements (Verdugo et al. 2007), the surface brightness of the extended shell has already been calibrated. However, for the emission core that is essentially a point source a series of corrections (aperture, flux, and color corrections) needs to be applied. Thus, we separated the structure into two parts – the extended shell and the emission core – and performed photometry separately. For the emission core, we followed a method of aperture photometry elucidated by Shirahata et al. (2009) and evaluated flux correction factors. For the extended shell, we simply integrated the surface brightness over the shell. However, a care was taken not to double-count the flux component in the extended shell part that is accounted for as part of the core emission via aperture correction. For each flux value obtained for the core and shell, we independently applied color correction and obtained the final flux values, which are listed in Table 1.

[1] Available at http://www.ir.isas.jaxa.jp/AKARI/Observation/

[2] Available at http://ssc.spitzer.caltech.edu/postbcd/

For PSF calibration purposes, we also observed an M5 III giant β Gru (Engelke, Price, & Kraemer 2006) with *AKARI* on 2006 November 16 and an asteroid Ceres (Müller & Lagerros 2002) with *Spitzer* on 2008 February 17. The same instrumental/mapping set-up was used for both PSF observations, except for *Spitzer* observations, for which the photometry/moving-cluster-offset mode was used because Ceres is a moving target. With the observed PSF maps, deconvolution was performed using an IRAF[3] task *lucy*, which is based on the Lucy-Richardson algorithm. The average gain and read-out noise were computed for each map given the documented detector responsivity for FIS and MIPS, integration time, and the averaged number of sky-coverage per pixel. Corresponding deconvolved images are shown in the bottom row of Figure 1 and in the bottom-left frame of Figure 2.

4. Results: the Extended Dust Shell of R Cas

Both *AKARI* (Figure 1) and *Spitzer* (Figure 2) images of R Cas look very much extended, while the faint surface brightness in the shell becomes progressively harder to make out in the *AKARI* LW bands, especially at 160μm. The radial surface brightness profile centered at the position of the star yielded 3′ to 4′ radius for the *AKARI* SW bands and *Spitzer* 70μm band and about 2′ radius for the *AKARI* LW bands (at $3\sigma_{\rm sky}$; Table 1). While the position of the star is obviously off-centered, the extended shell is roughly circular whose $3\sigma_{\rm sky}$ radius is 2.′3 to 2.′8 at 65, 70, and 90μm. To clarify we also note that the *AKARI* SW band images (N60 and WIDE-S) are affected by the cross-talk of the FIS detector that manifests itself as a linearly extended emission structure emanating from the central source into the position angles at 48° and 228° E of N (Shirahata et al. 2009).

The shell's emission structure consists of the relatively flat "plateau" region on the west side (of surface brightness ∼ 15 to 20 MJy sr^{-1} at 65 to 90μm and < 10 MJy sr^{-1} at 140μm) and the region of higher surface brightness (emission core) on the east side around the central star. This particular emission structure, however, does not appear to be caused by the off-centered central star. The deconvolved maps in the *AKARI* SW bands (the bottom-left images in Figure 1) and in the PSF-subtracted *Spitzer* 70μm band (the bottom-left image in Figure 2) all show consistently that the surface brightness is enhanced along a relatively well-defined rim that goes around the periphery of the shell for almost half the shell on its east side.

Assuming that the detected far-IR emission is mostly of dust continuum, the surface brightness enhancement on the east side can be caused by either the density or temperature enhancement of dust grains in the shell (or both). This is because in such an optically thin environment at far-IR the surface brightness S_ν is proportional to $\tau_\nu B_\nu(T)$, where τ_ν is optical depth along the line of sight and $B_\nu(T)$ is the blackbody function for dust grains at the temperature T. Thus, we fit the $\tau_\nu B_\nu(T)$ curve with the measured surface brightnesses at 65, 70, and 90μm to infer the dust temperature $T_{\rm dust}$ and the optical depth at 70μm, $\tau_{70\mu{\rm m}}$ simultaneously at each pixel. This was done by rescaling the *Spitzer* 70μm map to the same pixel scale as the *AKARI* SW band images (15″ pixel^{-1}) and performing the fitting using PSF-subtracted maps. The results are shown in the right frames of Figure 2.

[3] IRAF is distributed by the National Optical Astronomy Observatories, which are operated by the Association of Universities for Research in Astronomy, Inc., under cooperative agreement with the National Science Foundation.

The dust temperature map (the top-right frame of Figure 2) shows the peripheral enhancement similar to the one seen in the (deconvolved) surface brightness maps (the bottom frames of Figure 1). The dust temperature is the highest (> 20K) in the well-defined peripheral rim on the east side of the shell and in the less well-defined, clumpier structures on the west side. However, the $\tau_{70\mu{\rm m}}$ map (the bottom-right frame of Figure 2) does not show any obvious enhancement near the periphery of the shell. This suggests that the observed surface brightness enhancement in the extended shell of R Cas is due to the temperature enhancement in the shell rather than the density enhancement. What would cause such a temperature enhancement in the shell, then?

Vlemmings et al. (2003) measured proper motion of R Cas, $(\mu_\alpha, \mu_\delta) = (80.52 \pm 2.35, 17.10 \pm 1.75)$ mas yr^{-1}, by VLBI astrometry. This translates to the position angle of 78.°0 ± 1.°6 east of north, which agrees remarkably well with the direction along which there is a positive gradient of surface brightness. In other words, the emission structure of the extended shell appears to show mirror symmetry with respect to a line defined by the direction of proper motion. Interestingly, the direction of the measured proper motion is parallel to the direction of the apparent shift of the central star from the geometric center of the shell. The shape of the circumstellar shell was fit by an ellipse using the MIPS 70μm map, in which the pixel resolution is the highest. We defined the shell edge at the $3\sigma_{\rm sky}$ level and measured the radius (the distance from the star to the edge) in all directions at a certain azimuthal interval. The best-fit semi-major axis length (a) and eccentricity (ϵ) were thus searched for by adjusting these two values while minimizing the difference between the measured shape and the ellipse defined by the particular (a, ϵ) pair. During this fit, we assumed that the central star would fall on one of the foci and the semi-major axis would lie along the vector defined by the direction of the measured proper motion.

The best-fit semi-major axis and eccentricity pair, (a, ϵ), turned out to be $a = 165.''3$ and $\epsilon = 0.3$ (hence, the semi-minor axis length $b = 157.''7$): indeed, the extended shell of R Cas is not quite circular in projection. According to this best-fit ellipse, the distance from the ellipse center to one of the foci is $c = a \times \epsilon = 48.''8$. This means that the central star is 48.″8 displaced from the ellipse center over the course of the shell expansion. At the preferred distance for R Cas, 176 pc (Vlemmings et al. 2003), the semi-major and semi-minor axes correspond to 0.13 to 0.14 pc. If we assume that the measured CO expansion rate of 12 km s^{-1} (Bujarrabal, Fuente, & Omont 1994) is the (constant) expansion velocity of the extended dust shell, the crossing time of the shell is therefore roughly 10^4 years.

If the elongation of the R Cas shell is solely due to the motion of the central star with respect to the shell (in an otherwise stationary local environment), the star must have been moving roughly at 5 mas yr^{-1}, which is much less than the observed proper motion of 82.3 mas yr^{-1}. Thus, the elliptical elongation of the shell and the offsetting of the central star do not seem to be self-inflicted, as in the case where a pile-up of AGB wind material occurs at the interface between fast and slow AGB winds and defines the edge of the observed shell (Steffen et al. 1998). Rather, we speculate that the shell shaping is orchestrated by the interactions between the AGB winds and ambient ISM, as in the AGB wind-ISM interaction discovered around an AGB star, R Hya, by *Spitzer* (Ueta et al. 2006). In this scenario, the temperature enhancement seen in the east side of the shell is due to dust heating along the contact discontinuity between the AGB wind and the ISM flow. The temperature enhancement seen in

the west side is then probably due to dust heating in the wake of the AGB wind-ISM interactions flowing downstream (e.g. Wareing et al. 2007). This dust heating is likely due to collisions rather than shock emission because there is no known Hα emission source at the position of R Cas (Finkbeiner 2003). This interpretation is consistent with recent H I observations of R Cas (Matthews & Reid 2007), which identifies a head-and-tail structure whose alignment in the western wake of our far-IR maps is nearly perfect .

Unlike the R Hya case, however, we do not see any clear parabolic bow shock structure that is expected to arise at the interface between the AGB wind and ISM. Still, we recognize rather round temperature-enhanced regions toward the windward direction in the shell and wake-like temperature-enhanced structures toward the leeward direction. This is similar to the bow shock of Betelgeuse, for which its bow shock appears rather circular due to the inclination angle of the shock surface (Ueta et al. 2008). Assuming momentum conservation across a physically thin (i.e. radiative-cooling dominating) shock interface between the AGB wind and ISM, one can express the bow shock shape analytically as a function of the latitudinal angle θ measured from the apex of the bow with respect to the position of the central star as follows (Wilkin 1996):

$$R(\theta) = R_0 \frac{\sqrt{3(1-\theta\cot\theta)}}{\sin\theta} \tag{1}$$

where R_0 is the *stand-off distance* between the star and bow apex defined as

$$R_0 = \sqrt{\frac{\dot{M}v_{\rm w}}{4\pi\rho_{\rm ISM}v_*^2}} \tag{2}$$

for which $\dot{M}$ is the rate of mass loss, $v_{\rm w}$ is the isotropic stellar wind velocity, $\rho_{\rm ISM}$ is the ambient ISM mass density, and v_* is the space velocity of the star. Because the observed enhancement in the shell (i.e. an inclined bow shock) represents a conic section of the bow shock paraboloid (in optically thin dust distribution the column density becomes the greatest at the cross section of the structure with the plane of the sky), we can determine the inclination angle by fitting the apparent shape of the bow shock with the analytical function and a given inclination angle (Ueta et al. 2008).

The best-fit of the Wilkin solution fitting yields the inclination of the bow shock to be $\theta_{\rm incl} = \pm(68^\circ \pm 2^\circ)$ and the position angle of $74^\circ \pm 2^\circ$. The inclination angle has a degeneracy because this fitting method alone would not determine if the structure is inclined to us or away from us with respect to the plane of the sky. Nevertheless, the direction of the relative motion of the AGB wind shell with respect to the ambient ISM determined from the apparent bow shock structure is very much different than inferred from the observed motion of the central star ($\theta_{\rm incl} = 18\overset{\circ}{.}4$ toward us at the position angle of $78\overset{\circ}{.}0$). The discordance between these two values can be resolved only by incorporating the idea that the ISM itself is flowing in a particular direction. In other words, the difference between the vector of the apparent (heliocentric) space motion of the central star $\mathbf{v}_{*,\odot}$ and the vector of the space motion of the star *relative* to the ambient ISM $\mathbf{v}_{*,\rm ISM}$ (as derived from the 3-D orientation of the shock structure) is the heliocentric flow vector of the ambient ISM $\mathbf{v}_{\rm ISM,\odot}$:

$$\mathbf{v}_{\rm ISM,\odot} = \mathbf{v}_{*,\odot} - \mathbf{v}_{*,\rm ISM}. \tag{3}$$

The stand-off distance of $1\overset{\prime}{.}4 \pm 0\overset{\prime}{.}1$ translates to 0.1pc at the adopted VLBI-measured distance of 176pc. Solving eq.(2) for $v_{*,\rm ISM}$ with known quantities ($\dot{M} = 5\times10^{-7}$ M$_\odot$ yr^{-1}, $v_{\rm w} = 12$ km s^{-1}, and $\rho_{\rm ISM} \approx 1.4 m_{\rm H} n_{\rm ISM}$, where $1.4m_{\rm H}$ is the average ISM particle mass and $n_{\rm ISM}$ is the ISM number density), we have

$$\mathbf{v}_{\rm ISM,\odot} = \begin{pmatrix} v^{\rm rad}_{\rm ISM,\odot} \\ v^{\alpha}_{\rm ISM,\odot} \\ v^{\delta}_{\rm ISM,\odot} \end{pmatrix} = \begin{pmatrix} -22.9 \\ +67.4 \\ +14.3 \end{pmatrix} - \frac{1}{\sqrt{n_{\rm ISM}}} \begin{pmatrix} \pm33.0 \\ +12.6 \\ +3.6 \end{pmatrix} \ (\text{km s}^{-1}) \tag{4}$$

as a function of the remaining unknown, $n_{\rm ISM}$. The $\mathbf{v}_{\rm ISM,\odot}$-$n_{\rm ISM}$ relation suggests that $v_{\rm ISM,\odot}$ reaches its minimum of 55.6 km s^{-1} at $n_{\rm ISM} = 0.58$ cm^{-3} when the bow shock cone points to us and 72.5 km s^{-1} at $n_{\rm ISM} = 75.5$ cm^{-3} when the bow shock cone points away from us. In general, high values are unlikely for both $\mathbf{v}_{\rm ISM,\odot}$ and $n_{\rm ISM}$. Therefore, the case where the bow shock cone points away from us seems unlikely. If this is true the direction of the ISM flow should be going into the plane of the sky (positive $v_{\rm rad}$), given the space motion of the central star. Hence, the ambient ISM number density needs to be less than 2 cm^{-3}, which is in line with the fact that a relatively higher $n_{\rm ISM}$ value is expected for R Cas, a low galactic latitude object.

In the frame of stellar winds at 12 km s^{-1} (Knapp et al. 1998), the relative velocity of the ambient ISM flow into the interface regions is $12 + 35.5/\sqrt{n_{\rm ISM}}$ km s^{-1}, which translates into at least 37 km s^{-1} if $n_{\rm ISM} > 2$ cm^{-3}. Such a velocity could induce relatively weak (collisional) shock interactions that can raise the dust temperature of the AGB wind-ISM interface regions to $\sim 20-30$ K as seen from the present far-IR data. Given the nature of the central star, it is highly unlikely that dust heating is solely due to radiation from the central star. Typically the ambient interstellar radiation field is thought to contribute in heating dust grains in the outermost regions of the extended circumstellar shells. The present analysis of the far-IR data indicates that the AGB wind-ISM interactions can contribute as yet another source for dust heating in an otherwise cold environment. In future radiative transfer studies with our far-IR data sets, we will quantify relative contributions of these dust heating sources at the periphery of the extended dust shells around evolved stars as they would impact the physical and chemical conditions of the AGB wind ejecta upon injection into the ISM.

The dust temperature and optical depth maps together with a surface brightness map would yield crude estimates of dust mass in the shell:

$$M_{\rm dust} \approx \frac{F_\nu \lambda^2 D_*^2}{2kT_{\rm dust}\kappa_\nu} \quad \text{or} \quad \frac{\sum \tau_{\nu,{\rm i}} A_{\rm i}}{\kappa_\nu} \tag{5}$$

where F_ν is the measured flux at a given frequency ν of the band, λ is the wavelength of the band, D_* is the distance to the source, k is Boltzmann constant, κ_ν is the dust opacity, $A_{\rm i}$ is the area subtended by each pixel, and the summation over pixel i refers to integration over the shell. Here, we assume a spherical grain (0.1μm radius) of olivine ($MgFeSiO_4$; Dorschner et al. 1995) and calculated its opacity with Mie theory (48, 41, and 25 cm^2 g^{-1} at 65, 70, and 90μm, respectively) and use the adopted distance to R Cas of 176 pc. Our data then suggest that the dust mass in the shell is roughly $1-5\times10^{-5}$ M$_\odot$. Given the mass loss rate of 5×10^{-7} M$_\odot$ yr^{-1} and the dynamical age of the shell of $\sim 10^4$ years, the rough estimate of the total mass in the shell is 5×10^{-3} M$_\odot$, yielding the gas-to-dust ratio between 100 and 500. The amount of total mass estimated this way is a lower limit because the duration of mass loss could have been more than 10^4 years. Then, the estimated gas-to-dust ratio will be correspondingly higher, indicating that there exists less dust in a colder environment of the extended dust shells. However, this is based on a very rough estimate and needs to be confirmed by

radiative transfer calculation incorporating at least dust heating by the interstellar radiation field.

5. Conclusion

We obtained far-IR images of an oxygen-rich Mira variable R Cas at 65, 70, 90, 140, and 160μm using *AKARI* and *Spitzer* and revealed its very extended (2′ to 3′ radius, corresponding to 0.1 pc at its adopted distance of 176 pc), slightly elliptical ($\epsilon = 0.3$) dust shell, in which the central star is located offset from the geometric center of the shell in the direction of the measured proper motion of the central star. We recognize a positive gradient of the surface brightness along the direction of the "shift" of the central star, which apparently is caused by the surface brightness enhancement along the periphery of the shell in the east side seen in deconvolved images.

Fitting of the surface brightness using data in the 3 shortest bands suggests that the observed enhancement is caused by the temperature enhancement rather than the density enhancement, prompting a need to warm up dust grains primarily on the east side of the outer rim. Given the coincidence between the direction of the proper motion of the central star and the direction of the apex of the peripheric surface brightness/temperature enhancement in the shell, we infer that the observed shell structure represents the contact surface of the AGB wind-ISM interaction which is inclined to give an overall spherical shape instead of a typical parabolic bow shock structure. This AGB wind-ISM (collisional) interaction therefore warm up dust grains in the interface regions, causing the temperature enhancement towards the windward direction of the shell. Using the maps, we also estimated the total dust mass in the shell to be $1 - 5 \times 10^{-5}$ $M_\odot$.

The shape of the observed enhancement was fitted with the analytical function for the bow shock cone to derive the inclination angle of 68°. The apex vector of the bow shock cone and the space motion vector of proper motion of the central star were compared to deduce that there is an ISM flow local to R Cas that has a flow velocity of at least 55.6 km s^{-1}. Then, the relative velocity of the ambient ISM flow with respect to the AGB wind-ISM interface regions is at least 37 km s^{-1}. Therefore, such weak shocks can play a role in heating dust grains in the outermost regions of these extended dust shells around evolved stars in addition to the interstellar radiation field that is originally expected to play a role in an environment where luminosity from the central source is not enough for required dust heating.

Acknowledgements. We are grateful for financial support from the Institute of Space and Astronautical Science under the auspices of the Japan Aerospace Exploration Agency as well as the Jet Propulsion Laboratory/California Institute of Technology.

References

Bauer, W. H., & Stencel, R. E. 1994, AJ, 107, 2233
Bujarrabal, V., Fuente, A., & Omont, A. 1994, A&A, 285, 247
Deutsch, A. 1956, ApJ, 123, 210
Dorschner, J., Begemann, B., Henning, T., Jaeger, C., & Mutschke, H. 1995, A&A, 300, 503
Engelke, C. W., Price, S. D., & Kraemer, K. E. 2006, AJ, 132, 1445
Finkbeiner, D. P. 2003, ApJS, 146, 407
Gustafsson, B. & Höfner, S. 2004, Atmospheres og AGB Stars, in Asymptotic Giant Branch Stars, ed. H. J. Habing & H. Olofsson (Springer, New York), 149
Haniff, C. A., Scholz, M., & Tuthill, P. G. 1995, MNRAS, 276, 640
Hofmann, K.-H., Balega, Y., Scholz, M. & Weigelt, G. 2001, A&A, 376, 518
Izumiura, H., Waters, L. B. F. M., de Jong, T., et al. 1997, A&A, 323, 449
Kawada, M., Baba, H., Barthel, P. D., et al. 2007, PASJ, 59, 389
Knapp, G. R. & Morris, M. 1985, ApJ, 292, 640
Knapp, G. R., Pourbaix, D., Platais, I., & Jorissen, A. 2003, A&A, 403, 993
Knapp, G. R., Young, K., Lee, E., & Jorissen, A. 1998, ApJS, 117, 209
Kukarkin, B. V., Kholopov, P. N., Efremov, Yu. N., et al. 1996, General Catalog of Variable Stars 3rd Ed. (Moscow, U.S.S.R. Academy of Sciences)
Makovoz, D., Roby, T., Khan, I., & Booth, H. 2006, in Proceedings of the SPIE Vol. 6274: Advanced Software and Control for Astronomy, eds. H. Lewis & A. Bridger (Bellingham: SPIE), 10
Martin, D., Seibert, M., Neill, J. D., et al. 2007, Nature, 448, 780
Matthews, L. D., & Reid, M. J. 2007, AJ, 133, 2291
Meixner, M., Ueta, T., Dayal, A., et al. 1999, ApJS, 122, 221
Müller, T. G., & Lagerros, J. S. V. 2002, A&A, 381, 324
Murakami, H., Baba, H., Barthel, P., et al. 2007, PASJ, 59, 369
Perryman, M. A. C., Lindegren, L., Kovalevsky, J., et al. 1997, A&A, 323, L49
Pourbaix, D., Platais, I., Detournay, S., et al. 2003, A&A, 399, 1167
Rieke, G., Young, E. T., Engelbracht, C. W., et al. 2004, ApJS, 154, 25
Shirahata, M., Matsuura, S., Hasegawa, S., et al. 2009, PASJ, 6 737
Steffen, M., Szczerba, R., & Schönberner, D. 1998, A&A, 337, 149
Stencel, R. E., Pesce, J. E., & Bauer, W. H. 1988, AJ, 95, 141
Ueta, T. 2008, ApJ, 687, L33
Ueta, T., Speck, A. K., Stencel, R. E., et al. 2006, ApJ, 648, L39
Ueta, T., Izumiura, H., Yamamura, I., et al. 2008, PASJ, 60, S407
van Leeuwen, F. 2007, A&A, 474, 653
Verdugo, E., Yamamura, I., & Pearson, C. P. 2007, AKARI FIS Data User Manual Version 1.3
Villaver, E., García-Segura, G., & Manchado, A. 2003, ApJ, 585, 49
Vlemmings, W. H. T., van Langevelde, H. J.. Diamond, P. J., Habing, H. J., & Schilizzi, R. T. 2003, A&A, 407, 213
Wareing, C. J., Zijlstra, A. A., & O'Brien, T. J. 2007, MNRAS, 382, 1233
Werner, M. W., Roellig, T. L., Low, F. J., et al. 2004, ApJS, 154, 1
Wilkin, F. P. 1996, ApJ, 459, L31
Young, K., Phillips, T. G., & Knapp, G. R. 1993, ApJS, 86, 517

[1] Department of Physics and Astronomy, University of Denver, 2112 E. Wesley Ave., Denver, CO 80208, USA
[2] Institute of Space and Aeronautical Science, Japan Aerospace Exploration Agency, 3-1-1 Yoshinodai, Sagamihara, Kanagawa 229-8510, Japan
[3] Max-Planck-Institut für Extraterrestrische Physik, Giessenbachstraat 1, 85748 Garching, Germany
[4] Leiden Observatory, Leiden University, PO Box 9513, 2300 RA Leiden, The Netherlands
[5] Okayama Astrophysical Observatory, National Astronomical Observatory, Kamogata, Asakuchi, Okayama 719-0232, Japan
[6] Institute of Astronomy, School of Science, University of Tokyo, 2-21-1 Osawa, Mitaka, Tokyo 181-0015, Japan
[7] Department of Physics and Astronomy, University College London, Gower Street, London WC1E 6BT, UK
[8] Mullard Space Science Laboratory, University College London, Holmbury St. Mary, Dorking, Surrey RH5 6NT, UK
[9] National Astronomical Observatory of Japan, 2-21-1 Osawa, Mitaka, Tokyo 181-8588, Japan
[10] Kiso Observatory, Institute of Astronomy, School of Science, University of Tokyo, Mitake, Kiso, Nagano, 397-0101, Japan
[11] Department of Physics & Astronomy, University of Missouri, Columbia, MO 65211, USA

Table 1. Characteristics of the Far-IR Observations of R Cas with *AKARI* and *Spitzer*

Date & Time (UT)	Band	λ (μm)	$\Delta\lambda$ (μm)	Pixel Scale (arcsec)	Sky Coverage (pixel^{-1})	$S_{\nu,\mathrm{sky}}$ (MJy sr^{-1})	σ_{sky} (MJy sr^{-1})	$R_{3\sigma}$ (arcmin)	F_ν (Jy)
AKARI/FIS Observations									
2007 Jan 16 10:19	N60	65	22	15	6	8.7	1.2	3.1	121.48±19.90
	WIDE-S	90	38	15	9	8.6	0.6	3.8	73.42±10.03
	WIDE-L	140	52	30	15	13.2	1.3	2.0	25.89±2.09
	N160	160	34	30	10	9.9	1.3	1.8	22.41±7.47
Spitzer/MIPS Observations									
2008 Feb 18 04:02	MIPS70	70	19	4.92	9	10.0	1.1	3.5	...

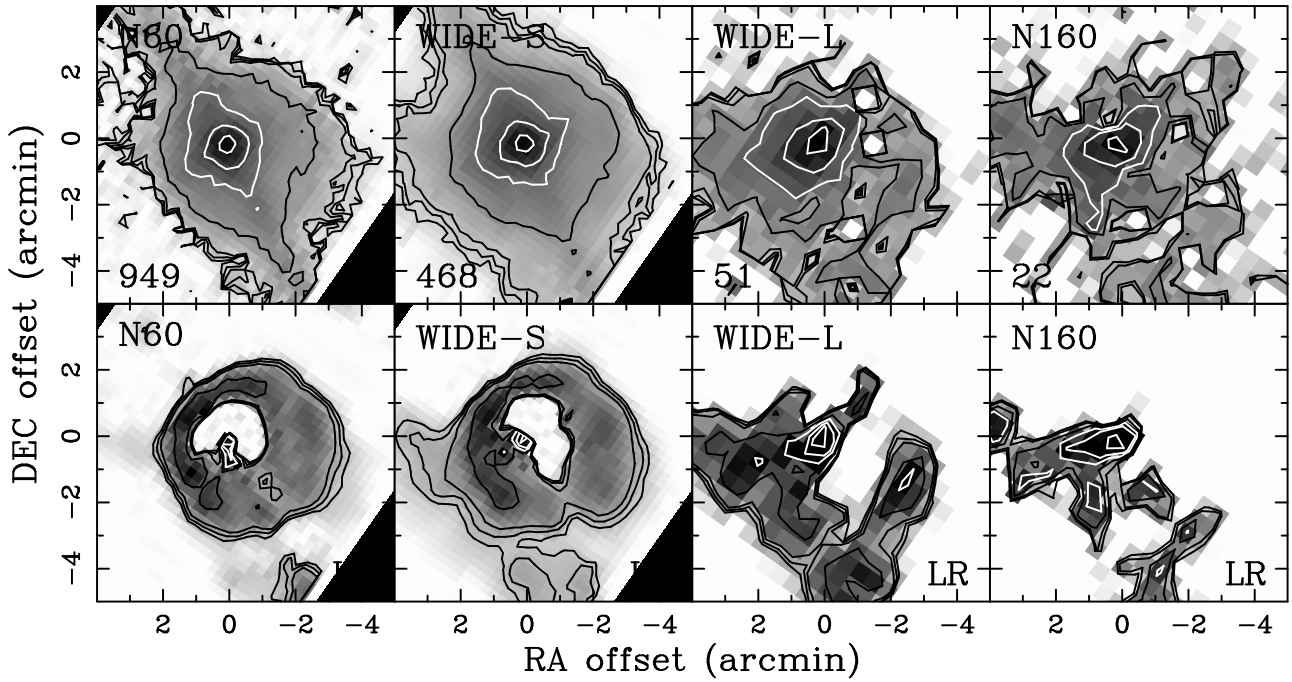

Fig. 1. AKARI/FIS maps of R Cas in the SW bands – N60 (65μm) and WIDE-S (90μm) at 15″pixel^{-1} scale – and in the LW bands – WIDE-L (140μm) and N160 (160μm) at 30″pixel^{-1} scale – in the top row from left to right, respectively. Background emission has been subtracted by a combination of temporal filters during data reduction. RA and DEC offsets (with respect to the stellar peak) are given in arcminutes. The number at the bottom left indicates the peak surface brightness in MJy sr^{-1}. The log-scaled grayscale surface brightness is contoured at 90, 70, 50 (in white), 30, 10, 3, and 1σ_{sky}. North is up, and east to the left. Images in the bottom row show deconvolved maps at corresponding wavelengths, for which "LR" on the bottom right indicates the Lucy-Richardson algorithm used.

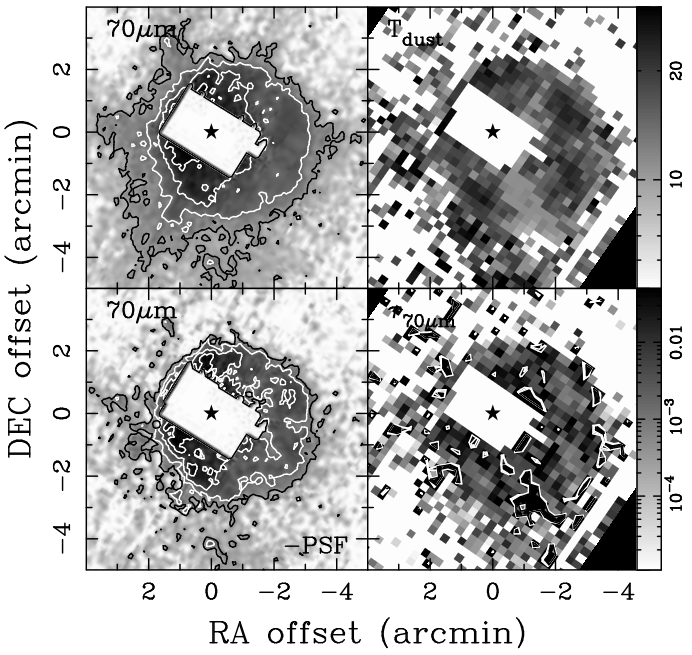

Fig. 2. Spitzer/MIPS map of R Cas in the 70μm band at 4″92 pixel^{-1} scale (top left frame) and its PSF-subtracted image (bottom left frame). Background emission has been subtracted by a combination of temporal filters during data reduction. RA and DEC offsets (with respect to the position of the star, indicated by the "star" symbol) are given in arcseconds. Also shown are the dust temperature (top right) and optical depth (at 70μm; bottom right) maps derived from the fitting of the shortest 3 waveband images (65, 70, and 90μm) under the assumption of optically thin dust emission. The wedges on the right indicate the log-scaled dust temperature in K (top) and optical depth at 70μm (bottom). North is up, and east to the left.

R Cas

List of Objects

'R Cas' on page 7